Check for updates

RESEARCH ARTICLE

NANO · MICRO small
www.small-journal.com

Modulating Oxygen Evolution Reaction Pathways via (Oxy)Hydroxide-Driven Surface Reconstruction on Ti_3C_2 MXene Electrocatalysts

Nur Aqlili Riana Che Mohamad, Hyunjeong Lee, Mingming Gong, Caichao Ye, Yunfei Bu, Zhiqun Lin, Dong-il Won, Jeongwon Kim, Filipe Marques Mota,* and Dong Ha Kim**

The oxygen path mechanism (OPM) has gained increasing interest as an oxygen evolution reaction (OER) pathway with facile O–O coupling. Importantly, OPM differs from both adsorbate evolution (AEM) and lattice oxygen mechanism (LOM) routes, which involve multiple intermediates and lattice oxygen, respectively. Here, an electro-activated reduced Ti_3C_2 MXene (rTi_3C_2) system is introduced that modulates the OER pathway by governing the population of (oxy)hydroxide species on rTi_3C_2 surfaces. Through *operando* Raman spectroscopy, the in situ formation of (oxy)hydroxide species on rTi_3C_2 surfaces (rTi_3C_2-T) is evidenced during electro-activation, promoting OER active-site evolution through rational surface reconstruction. The increased (oxy)hydroxide concentration induces a 27% reduced OER overpotential at 10 mA cm^{-2} and a 67% current density increment at high voltages against the Ti_3C_2 reference. *Operando* vibrational spectroscopy and direct probing measurements offer insight into the dynamic reconfiguration of rTi_3C_2-T surfaces, the nature of reaction intermediates, and, most importantly, into the transition from AEM to OPM routes during OER. First-principles calculations further validate a cooperative catalysis pathway with reduced energy barrier, corroborating the enhanced activity of (oxy)hydroxide-rich MXene catalysts. These findings underscore the potential of electrochemically-assisted surface engineering to promote the OPM pathway and substantially improve OER through selective surface modification.

1. Introduction

MXenes, a class of 2D transition metal carbides, have emerged as highly tunable materials for energy storage and conversion, offering exceptional metallic conductivity, structural robustness, and chemically versatile surfaces.[1,2] Defined by the general formula $M_{n+1}X_nT_x$ (M = transition metal, X=C or N, T = surface functional groups), MXenes allow control over electronic structure and charge transfer kinetics. Ti_3C_2 has demonstrated broad applicability in rechargeable batteries, (photo)electrocatalysis, solar energy harvesting, and environmental remediation,[3,4] with recent studies further reinforcing its role in advancing multifunctional energy technologies.[5,6] Despite performance limitations of its pristine form (e.g., restacking behavior and insufficient intrinsic catalytic activity), it is now well understood that these hindrances can be effectively overcome through surface engineering or compositional tunings.[7,8]

N. A. R. Che Mohamad, H. Lee, Z. Lin, D.-il Won, J. Kim, D. H. Kim
Department of Chemistry and Nanoscience
Division of Molecular and Life Sciences
College of Natural Sciences
Ewha Womans University
52, Ewhayeodae-gil, Seodaemun-gu, Seoul 03760, Republic of Korea
E-mail: jeongwon.kim@northwestern.edu; dhkim@ewha.ac.kr

M. Gong, C. Ye
Academy for Advanced Interdisciplinary Studies &
Institute of Innovative Materials
Guangdong Provincial Key Laboratory of Computational Science and Material Design
Southern University of Science and Technology
Shenzhen, Guangdong 518055, P. R. China

Y. Bu
School of Environmental Science and Technology
UNIST-NUIST Energy and Environment Jointed Lab, (UNNU)
Nanjing University of Information Science & Technology
Pukou, Nanjing, Jiangsu 210044, P. R. China

Z. Lin
Department of Chemical and Biomolecular Engineering
National University of Singapore
Singapore 117585, Singapore

The ORCID identification number(s) for the author(s) of this article can be found under https://doi.org/10.1002/smll.202508259

© 2025 The Author(s). Small published by Wiley-VCH GmbH. This is an open access article under the terms of the Creative Commons Attribution-NonCommercial License, which permits use, distribution and reproduction in any medium, provided the original work is properly cited and is not used for commercial purposes.

DOI: 10.1002/smll.202508259

Strategic modulation of surface functional groups directly governs active-site availability and interfacial charge transfer, making MXenes attractive electrocatalysts, particularly for the kinetically hindered four-proton-coupled electron transfer in the oxygen evolution reaction (OER). Unraveling their electrocatalytic potential necessitates a deeper examination of the underlying reaction mechanisms. The conventional OER mechanism (**Scheme 1**), such as the adsorbate evolution mechanism (AEM), relies on sequential *OH, *O, and *OOH formation, where the rate-determining step (RDS) often involves *OH deprotonation or O—O bond formation.[9,10] While lattice oxygen participation in the lattice oxygen mechanism (LOM) can mitigate these limitations by introducing reversible oxygen vacancy (V_o) dynamics, the recently proposed oxide path mechanism (OPM) offers a more direct approach, enabling oxygen evolution via *O–O radical coupling without lattice oxygen involvement. The efficiency of OPM, however, is contingent on stringent geometric and electronic requirements at metal active sites, necessitating atomic-scale precision in catalyst design.[11] While dual-metal configurations have been explored to optimize O–O radical formation, achieving stable and well-defined active sites remains a formidable challenge. Emerging literature and mechanistic studies suggest that bimetallicity, while beneficial, is not a strict prerequisite for triggering the OPM.[12–14] Instead, the ability to regulate surface intermediate populations and to modulate the local electronic environment at active sites plays an equally critical role in determining the operative OER pathway. The incorporation of (oxy)hydroxide species particularly can dynamically restructure the interfacial electronic landscape and stabilize key reaction intermediates, thereby offering a viable strategy to optimize catalytic performance.[15,16]

Harnessing surface chemistry as a design principle, we demonstrate how (oxy)hydroxide-enriched Ti_3C_2 MXene modulates OER pathways. This regulation is achieved by tuning the surface (oxy)hydroxide content through a facile electrochemical strategy, enabling effective catalytic optimization. Electroactivation in alkaline media (0.1 M KOH) induces abundant (oxy)hydroxide species on reduced Ti_3C_2 substrate (rTi_3C_2-T), triggering surface reconstruction and significantly increasing the electrochemically active surface area by 43.1%. The incorporation of (oxy)hydroxide species in rTi_3C_2-T shifts the reaction toward the OPM pathway, contributing to a measurable reduction in overpotential by 27% at 10 mA cm^{-2} and enhancing OER activities at high voltage by 67%, highlighting the role of surface functionalization in accelerating OER kinetics. In contrast, pristine rTi_3C_2, lacking (oxy)hydroxide functionalization, predominantly follows the AEM/LOM pathway, constraining its catalytic efficiency. *Operando* Raman spectroscopy, coupled with direct intermediate probing, reveals distinct chemical transformations in rTi_3C_2-T, supporting its preferential engagement with the OPM mechanism. These structural and electronic modifications are further corroborated by first-principles calculations, which demonstrate that increasing (oxy)hydroxide content lowers the energy barrier for OPM, facilitating a more efficient reaction route (Scheme 1b). Beyond pathway regulation, these findings reveal that OER activity strongly correlates with (oxy)hydroxide composition, reaching peak performance when (oxy)hydroxide species are most abundant (Scheme 1c). By integrating *operando* spectroscopy with theoretical insights, this study demonstrates the role of surface functionalization in MXene-based OER catalysis, providing a framework for optimizing reaction dynamics through surface engineering.

2. Results and Discussion

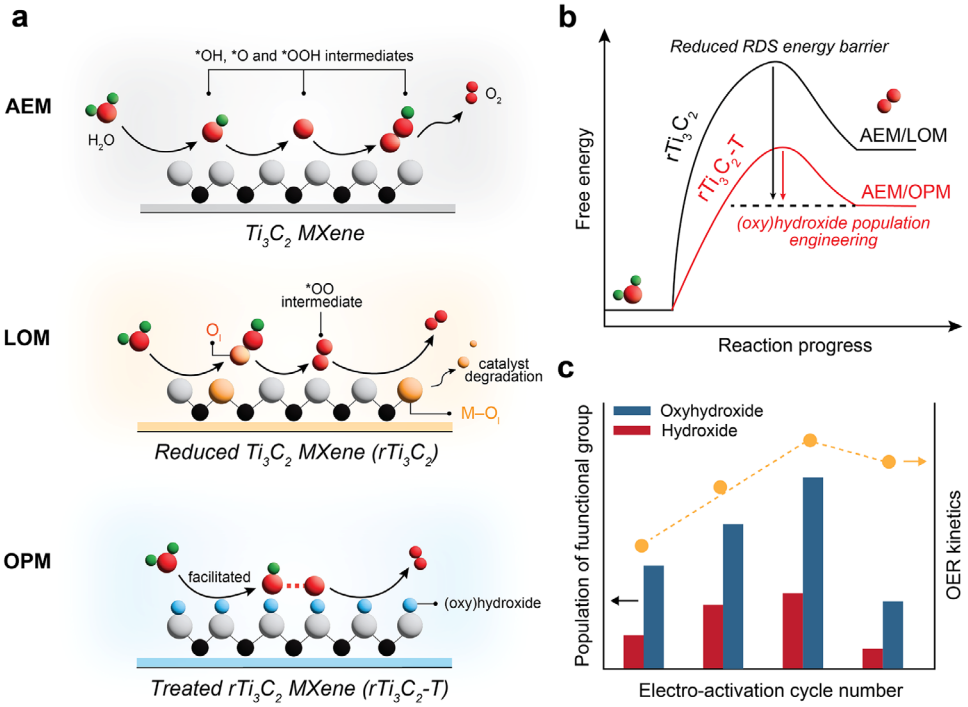
2.1. Materials Characterization

The synthesis route for Ti_3C_2 MXene, with details of the etching process of the MAX phase (Ti_3AlC_2) provided in the Supporting Information. After etching, the Ti_3C_2 MXene underwent hydrothermal exfoliation at 180 °C in a mild ascorbic acid solution for 3 h, with the resulting materials being denoted reduced Ti_3C_2 MXene (rTi_3C_2). A counterpart synthesized under extended reducing periods (6 h) was also prepared as a reference (Ex-rTi_3C_2). X-Ray diffraction (XRD) analysis first corroborated the successful removal of the Al layer, as the (104) peak of Ti_3AlC_2 at 39° nearly disappeared (**Figure 1a**). A noticeable broadening and downshift of (002) reflection at 9.8° suggested increased interlayer distance, promoting better electrolyte penetration and ion intercalation during redox processes.[17] The etching process disrupted hydrogen bonds and van der Waals forces, leading to expanded interlayer spacing as shown in the XRD pattern (Figure 1b). Raman spectroscopy (Figure 1c,d) showed characteristic vibrational modes in the 200–800 cm^{-1} range, with the peak at ≈205 cm^{-1} corresponding to Ti-C vibrations, and the region ≈230–470 cm^{-1} representing in-plane (E_g) vibrations of surface groups attached to Ti atoms. The range between 550 and 730 cm^{-1} is assigned primarily to carbon vibrations (both E_g and A_{1g}) and used for fingerprinting surface groups.[17–19] The D and G bands ≈1350 cm^{-1} and ≈1580 cm^{-1}, respectively, indicated graphitic carbon structures, highlighting structural disorder alongside retained graphitic domains, which contribute to improved electronic conductivity.[20]

J. Kim
Department of Chemistry
Northwestern University
Evanston, IL 60208, USA
F. Marques Mota
Department of Chemistry
School of Natural Sciences
University of Lincoln
Lincoln LN6 7TS, UK
E-mail: fmarquesmota@lincoln.ac.uk
D. H. Kim
College of Medicine
Ewha Womans University
25, Magokdong-ro 2-gil, Gangseo-gu, Seoul 07804, Republic of Korea
D. H. Kim
Graduate Program in Innovative Biomaterials Convergence
Ewha Womans University
52 Ewhayeodae-gil, Seodaemun-gu, Seoul 03760, Republic of Korea
D. H. Kim
Basic Sciences Research Institute (Priority Research Institute)
Ewha Womans University
Seoul 03760, Republic of Korea
D. H. Kim
Nanobio • Energy Materials Center (National Research Facilities and Equipment Center)
Ewha Womans University
Seoul 03760, Republic of Korea

© 2025 The Author(s). Small published by Wiley-VCH GmbH

16136829, 2025, 40, Downloaded from https://onlinelibrary.wiley.com/doi/10.1002/smll.202508259 by Ewha Womans University Library, Wiley Online Library on [13/01/2026]. See the Terms and Conditions (https://onlinelibrary.wiley.com/terms-and-conditions) on Wiley Online Library for rules of use; OA articles are governed by the applicable Creative Commons License



Scheme 1. a) Schematic representation of OER mechanisms on Ti_3C_2 MXene-based catalyst, highlighting the adsorbate evolution mechanism (AEM), lattice oxygen mechanism (LOM), and oxide path mechanism (OPM). AEM progresses through sequential $^*OH$, $^*O$, and $^*OOH$ formation, while LOM enables O—O bond formation via $^*O$–O radical coupling with lattice oxygen (O_l). The introduction of (oxy)hydroxide-rich surface on rTi_3C_2 MXene facilitates the OPM pathway, enhancing oxygen evolution. b) Theoretical calculations reveal that the enriched (oxy)hydroxide surface enhances the AEM and OPM pathways by facilitating electron transfer during the rate-determining step (RDS), thereby lowering the energy barrier for oxygen evolution. In contrast, high oxygen vacancy concentrations in rTi_3C_2 MXene predominantly follow AEM and LOM pathways with higher energy barriers, leading to reduced catalytic activity. c) *Operando* Raman analysis reveals the electro-activation of rTi_3C_2 MXene in alkaline solution, observing progressive (oxy)hydroxide formation over multiple cycles.

To gain deeper insight into the surface properties of these materials, we further compared the collected Fourier transform infrared (FT-IR) spectra (Figure 1e). The etched Ti_3C_2 MXene exhibited Ti–F bending modes at ≈770 cm^{-1},[21] C—F stretching at ≈1160 cm^{-1},[22] O—H stretching near ≈1380 cm^{-1}, and C-O stretching at ≈1630 cm^{-1}. In contrast, samples following treatment in the ascorbic acid solution showed a broadening and increased intensity of peaks in the 1700–1500 cm^{-1} region, attributed to enhanced C—O stretching and O—H bending vibrations.[23,24] Additionally, the C—F stretching peaks ≈1250 cm^{-1} range also broadened, indicating an increase in surface terminations at defect sites.[24] The N_2 adsorption–desorption isotherms (Figure 1f) revealed the specific surface area of the Ti_3C_2-based materials. The samples displayed Type II isotherms, characteristic of nonporous structures with unrestricted monolayer-multilayer adsorption. The rTi_3C_2 achieved a Brunauer–Emmett–Teller (BET)-specific surface area of 12.85 m^2 g^{-1} a threefold increase against the etched Ti_3C_2 (3.94 m^2 g^{-1}) and significantly higher than the Ti_3AlC_2 MAX phase (2.45 m^2 g^{-1}). This increased surface area enhanced the density of active sites, improving catalytic activity and ion exchange capabilities for energy conversion applications.

Figure 2 presents Scanning Electron Microscopy (SEM) and Transmission Electron Microscopy (TEM) images illustrating the morphological evolution of Ti_3C_2 during the hydrothermal process. Ti_3C_2 displayed its characteristic accordion-like structure (Figure 2a), which transformed into smaller and thinner fractions of rTi_3C_2 2D nanosheets (Figure 2b) following the hydrothermal treatment. This transformation aligns with the observed increase in BET surface area (Figure 2f). Extended hydrothermal treatment, however, led to densification of the rTi_3C_2 nanosheets (Ex-rTi_3C_2) (Figure 2c), resulting in a detrimental reduction in surface area. The corresponding EDS mapping further verified the distribution of Ti and C elements on both modified Ti_3C_2 nanosheets (Figure S1, Supporting Information). X-ray photoelectron spectroscopy (XPS) (Figure 2d–f) was conducted to analyze the chemical composition and surface states of all untreated and treated MXene materials. Deconvolution of the Ti *2p* spectra of Ti_3C_2 (Figure 2d) identified peaks corresponding to Ti–O (464.8 eV, 459.3 eV), Ti–F (462.5 eV, 455.9 eV), and Ti–C (461.1 eV, 454.7 eV). Meanwhile, the Ti–O peak intensity in rTi_3C_2, increased, with the Ti–F peak intensity diminished, indicating a shift in surface chemistry.[8,25,26] This shift suggests that F-terminated surface sites were replaced by O-terminated sites, as evidenced by a significant decrease in surface F content and a concurrent increase in surface O content.[27–29] The O *1s* spectra (Figure 2e) revealed peaks at 529.4, 531.5, 533.2, and 534.1 eV, attributed to M–O, oxygen vacancies, and Ti–C–O_x groups, respectively. These features indicate the formation of oxygen vacancies and –OH terminal groups on the MXene surface.[30,31] Additionally, a slight peak shift in rTi_3C_2 implies electron redistribution from oxygen atoms and the emergence of oxygen vacancies,

 © 2025 The Author(s). Small published by Wiley-VCH GmbH

16136829, 2025, 40, Downloaded from https://onlinelibrary.wiley.com/doi/10.1002/smll.202508259 by Ewha Womans University Library, Wiley Online Library on [13/01/2026]. See the Terms and Conditions (https://onlinelibrary.wiley.com/terms-and-conditions) on Wiley Online Library for rules of use; OA articles are governed by the applicable Creative Commons License

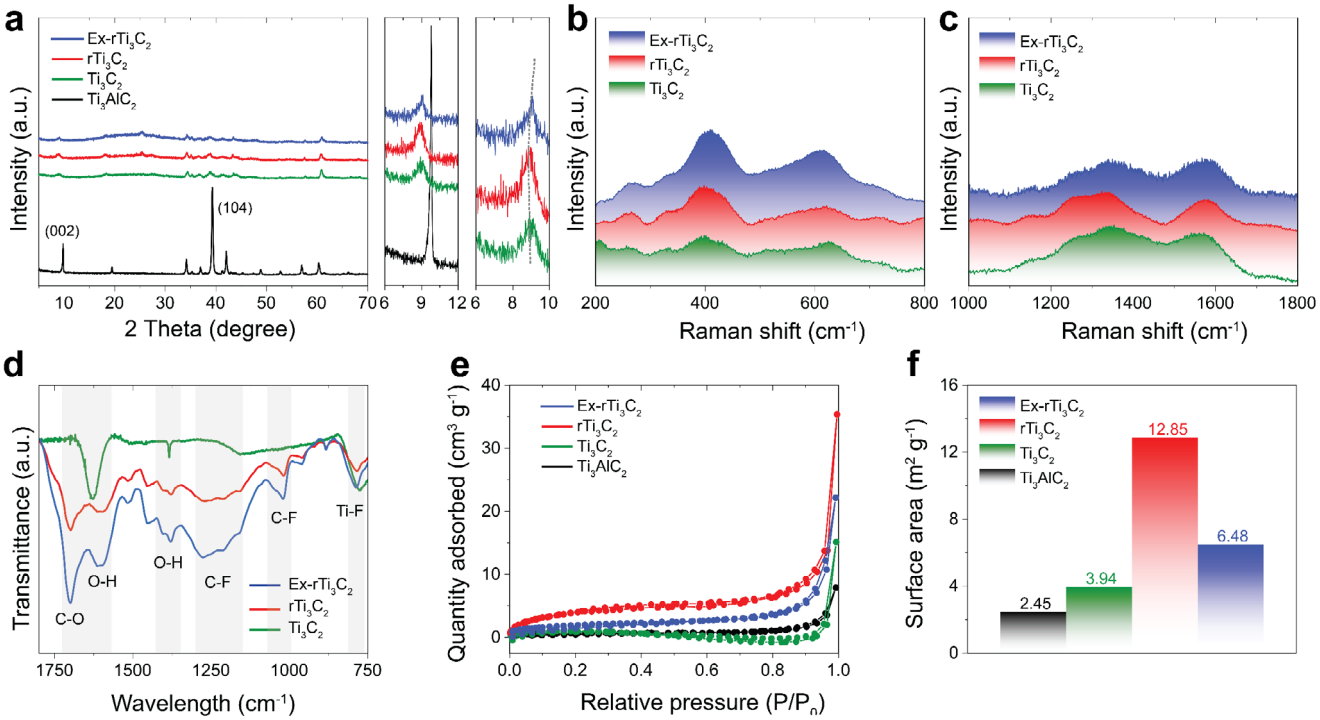


Figure 1. a) X-ray diffraction (XRD) patterns and magnified XRD pattern of $Ti_3Al_2C_2$, Ti_3C_2, rTi_3C_2, and Ex-rTi_3C_2 catalysts. Raman spectra of Ti_3C_2, rTi_3C_2, and Ex-rTi_3C_2 at(b) lower (200–800 cm^{-1}) and c) higher wavenumbers (1000–1800 cm^{-1}). d) FTIR spectra of Ti_3C_2, rTi_3C_2, and Ex-rTi_3C_2. e) The N_2 adsorption–desorption isotherm curves of $Ti_3Al_2C_2$, Ti_3C_2, rTi_3C_2, and Ex-rTi_3C_2 and f) the corresponding BET surface area.

leading to an increase in free electron density.[32] An enhanced C—O peak intensity in rTi_3C_2-T suggested an increased presence of oxygenated functionalities, which serve as active sites during electrochemical reactions.[33] Additionally, shifts in the F *1s* spectra (Figure 2f) indicated changes in Ti–F bonding, reflecting modifications in surface termination that could enhance interactions with electrolyte species.[34]

2.2. Electrochemical Measurements

The Ti_3C_2, rTi_3C_2, and Ex-rTi_3C_2 electrocatalysts underwent a subsequent electro-activation process from –0.1 to –0.4 V_{RHE} for 20 cycles in a 0.1 M KOH electrolyte using a three-electrode setup. The resulting materials were denoted as Ti_3C_2-T, rTi_3C_2-T, and Ex-rTi_3C_2-T, respectively. This treatment was targeted to induce surface changes of Ti_3C_2-based MXenes through polarization in the presence of non-reducible cations, at sufficiently negative potentials. These surface modifications can significantly influence electrode kinetics, the intrinsic activity and selectivity of catalysts, and redirect reaction mechanisms in electrocatalysis.[35,36] The OER activity of all MXene-based electrocatalysts was then assessed in a three-electrode setup in 0.5 M H_2SO_4 through linear sweep voltammetry (LSV) at a scan rate of 10 mV s^{-1} without *iR* corrections (**Figure 3a**). The LSV curves revealed improved catalytic activities for all treated MXenes, with rTi_3C_2-T showing the lowest OER overpotential at 10 mA cm^{-2} (≈0.65 V), representing an 11% reduction against the untreated counterpart (0.73 V) and a 27% reduction against the pristine Ti_3C_2. Our rTi_3C_2-T exhibited the highest Tafel slope (355 mV dec^{-1}) against the untreated rTi_3C_2 (296 mV dec^{-1}), suggesting alterations in the reaction mechanism after the cathodic treatment. The Tafel slope values for Ex-rTi_3C_2-T, Ex-rTi_3C_2, Ti_3C_2-T, and Ti_3C_2 were 271, 154, 260, and 212 mV dec^{-1}, respectively. We further examined the $\Delta\eta/\Delta$Log j ratio (Figure 3d) to evaluate the impact of mass transport and electron transfer. The treated catalysts displayed stable Tafel slope values over a broad range of current densities, indicating a reaction mechanism that is independent of potential. The rTi_3C_2-T, however, exhibited a distinct potential dependence, suggesting dynamic changes in its OER mechanism under varying potentials. Moreover, the gradual decrease in the $\Delta\eta/\Delta$Log j ratio at higher current densities for rTi_3C_2-T underscores its suitability for high-current applications, maintaining efficiency under elevated operational conditions. In contrast, Ex-rTi_3C_2 displayed a potential-dependent behavior with a gradual increase in the $\Delta\eta/\Delta$Log j ratio at high current densities, indicating fluctuations in its OER mechanism. This variability suggests that the reaction kinetics of Ex-rTi_3C_2 may be limited by mass transport effects.[37]

Electrochemical impedance spectroscopy (EIS) was utilized to determine the charge transfer resistance (R_{ct}) of the catalysts. The Nyquist plots (Figure 3e) revealed a smaller semicircle with rTi_3C_2-T, corresponding to the lowest R_{ct} and suggesting faster charge transfer during OER. This observation agreed with the lower OER overpotentials, supporting an enhanced electron transfer capacity at the surface of our rTi_3C_2-T. To further assess kinetic barriers, we evaluated temperature-dependent OER activities using Arrhenius plots (Figure 3f; Figure S2, Supporting Information). The rTi_3C_2-T showed an apparent activation energy of 13.7 kJ mol^{-1}, lower than that of reported

© 2025 The Author(s). Small published by Wiley-VCH GmbH

16136829, 2025, 40, Downloaded from https://onlinelibrary.wiley.com/doi/10.1002/smll.202508259 by Ewha Womans University Library, Wiley Online Library on [13/01/2026]. See the Terms and Conditions (https://onlinelibrary.wiley.com/terms-and-conditions) on Wiley Online Library for rules of use; OA articles are governed by the applicable Creative Commons License

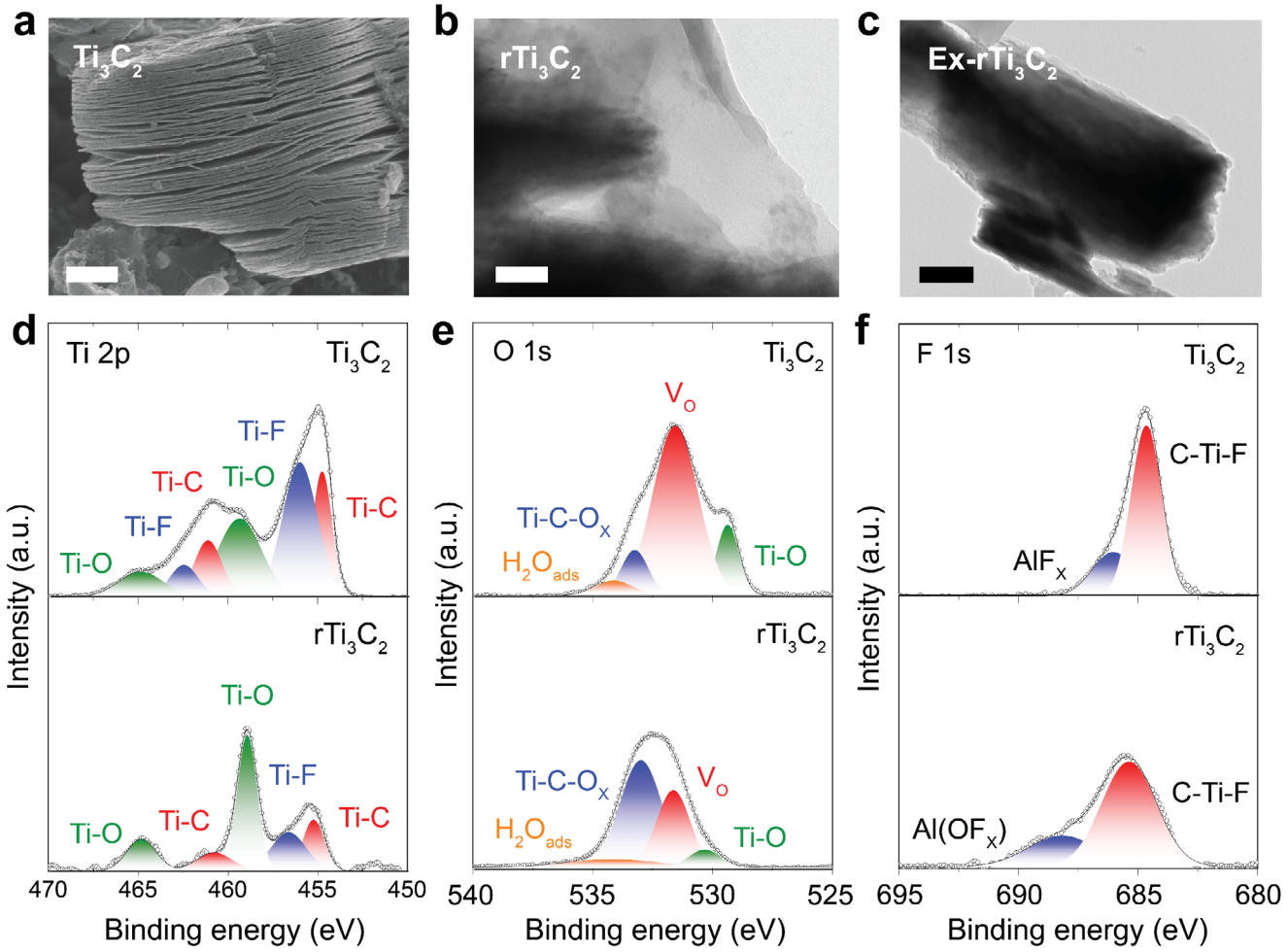


Figure 2. Scanning electron microscopy (SEM) images of a) Ti_3C_2 (scale bar is 1 µm). TEM images of b) rTi_3C_2 (scale bar is 0.1 µm) and c) Ex-rTi_3C_2 (scale bar is 0.2 µm). High resolution X-ray photoelectron spectroscopy (XPS) spectra of d) Ti *2p*, e) O *1s*, and f) F *1s* for Ti_3C_2 and rTi_3C_2 catalysts.

oxyhydroxide-contained electrocatalysts,[38,39] indicating a reduced kinetic barrier involved in the OER process. Electrochemically active surface areas (ECSA) were also measured through double-layer capacitance (C_{dl}) values obtained from cyclic voltammetry (CV) at scan rates between 20 and 100 mV s^{-1} in a non-faradaic region (Figure S3, Supporting Information). The treated catalysts revealed increased C_{dl} values ascribed in each case to an enlarged ECSA. In particular, rTi_3C_2-T showed the highest C_{dl} (49.9 mF cm^{-2}), representing a 43.1% increase following the conducted treatment. The enhanced ECSA aligns with the observed suppressions in overpotential and improvements in charge transfer, demonstrating the effectiveness of the cathodic treatment in exposing additional active sites.

2.3. In Situ Raman Spectroscopy Analysis

To shed light on the impact of the electro-activation process on the resulting electrocatalytic performance, our MXene electrocatalysts were characterized using in situ Raman spectroscopy. A custom-designed three-electrode Raman electrochemical cell (**Figure** 4a) was utilized 1) to capture real-time structural changes and offer in situ observation of surface species formed during the activation procedure of our rTi_3C_2 and 2) to assess the OER process, including long-term stability testing. Detailed procedures were summarized in the Supporting Information. In all cases, the Raman peak assignments for rTi_3C_2-T MXene were found to closely match the established spectral features of $Ti_3C_2T_x$, as reported by Gogotsi and colleagues.[19] These peaks were resolved using Gaussian fitting and attributed to surface groups such as =O, —(OH), and —O(OH).

Raman spectroscopy measurements (Figure 4b–e) were first conducted to monitor changes to the surface groups on rTi_3C_2-T, following cathodic sweeps from –0.1 to –0.4 V_{RHE} up to 40 cycles. The Raman band observed at 550 cm^{-1} was attributed to in-plane vibrations of C atoms in $Ti_3C_2O_2$, while Raman bands ≈600 and 730 cm^{-1} were assigned to out-of-plane C vibrations in the same phase. Additionally, the 650 cm^{-1} band was ascribed to in-plane vibrations of $Ti_3C_2(OH)_2$, and the prominent bands at 675 and 710 cm^{-1} were associated with in-plane and out-of-plane vibrations of C atoms in $Ti_3C_2O(OH)$, respectively.[19] To facilitate our understanding of surface group evolution analysis, we focused on key Raman-active groups, i.e., —(OH) and —O(OH), normalized against =O counterparts (Figure 4f). As observed,

© 2025 The Author(s). Small published by Wiley-VCH GmbH

16136829, 2025, 40, Downloaded from https://onlinelibrary.wiley.com/doi/10.1002/smll.202508259 by Ewha Womans University Library, Wiley Online Library on [13/01/2026]. See the Terms and Conditions (https://onlinelibrary.wiley.com/terms-and-conditions) on Wiley Online Library for rules of use; OA articles are governed by the applicable Creative Commons License

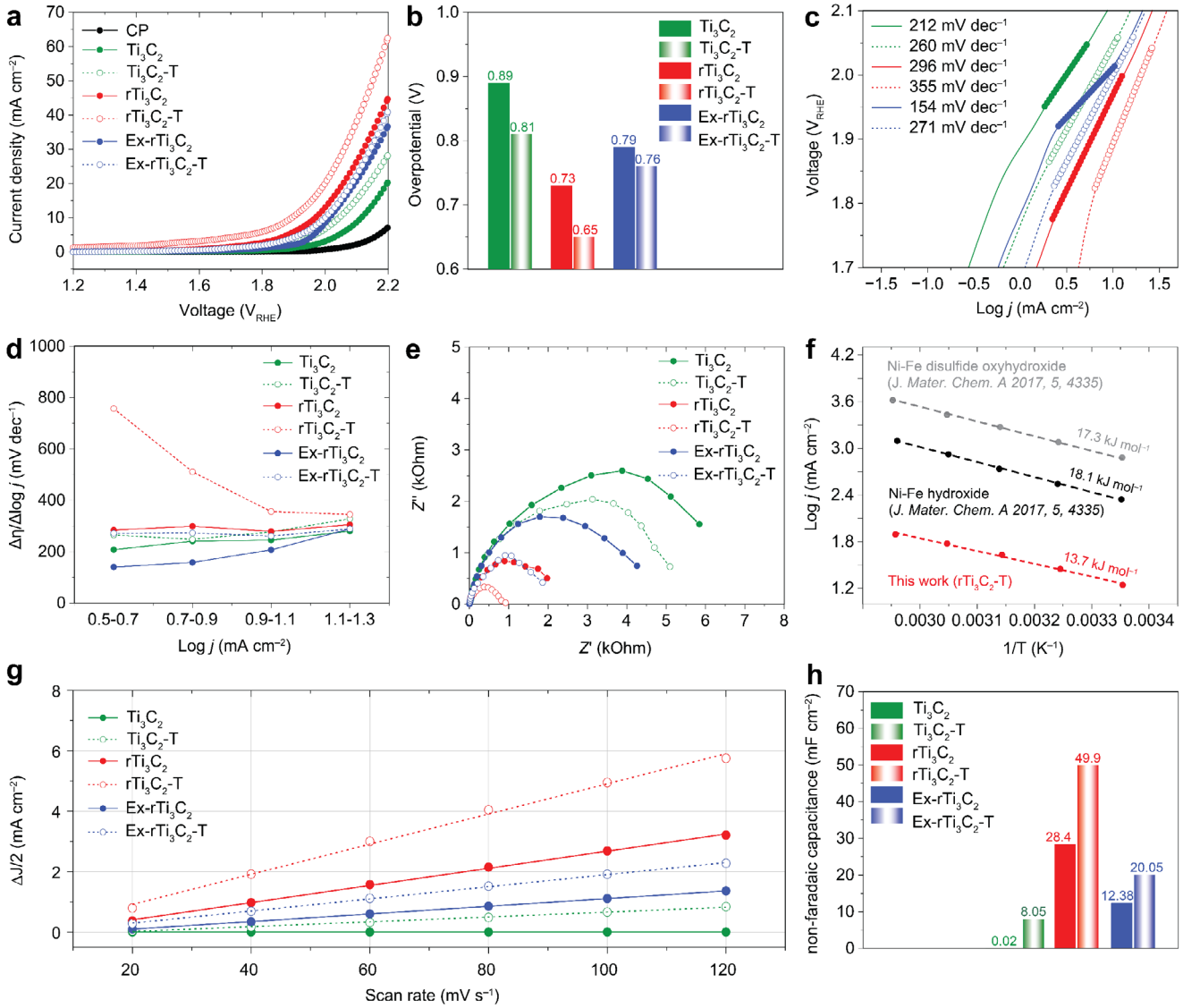


Figure 3. Electrocatalytic OER performance of Ti_3C_2, Ti_3C_2-T, rTi_3C_2, Ti_3C_2-T, Ex-rTi_3C_2 and Ex-rTi_3C_2-T catalysts in 0.5 M H_2SO_4 electrolyte. a) LSV curves and b) corresponding overpotential at 10 mA cm^{-2}. c) Tafel curves obtained from the LSV curves in (a). d) Ratios of $\Delta\eta/\Delta$Log j in various current density ranges and the Nyquist plots of prepared catalysts. f) The Arrhenius plots of r-Ti_3C_2-T electrode acquired at a current density of 10 mA cm^{-2} and comparison with Ni-Fe-based electrocatalysts.[38] g,h) The double-layer capacitance (C_{dl}) values obtained from cyclic voltammetry (CV) at scan rates between 20 and 100 mV s^{-1} in a non-faradaic region.

the concentration of —O(OH) species increased gradually, reaching a $I_{O(OH)}/I_O$ maximum of ≈2.5 at 20 cycles. Beyond 20 cycles, however, the surface was rapidly dominated by =O groups. Similarly, the ratio of —(OH) to =O increased during the first 20 cycles (I_{OH}/I_O maximum of ≈1.0), declining after this point. These results suggest that under the applied cathodic potential, hydroxyl ions (OH^-) from the alkaline electrolyte could be progressively intercalated into the rTi_3C_2 layers, facilitating the formation of $Ti_3C_2O(OH)$ and $Ti_3C_2(OH)_2$ species.[34,40] After 20 cycles, the decline in $Ti_3C_2O_2$ Raman bands verified its conversion into $Ti_3C_2O(OH)$ species. This was consistent with XPS spectra (Figure S4, Supporting Information), which show increased Ti–O and C–Ti–OH signals with SEM (Figure S5, Supporting Information) and TEM (Figure S6, Supporting Information) images verified unchanged morphology after 20 cycles, underscoring the material's structural stability during surface evolution. The resurgence of $Ti_3C_2O_2$ Raman bands after 40 cycles, however, reflected a dynamic surface restructuring following prolonged electrochemical cycling. This effect was attributed to the exposure of multilayer MXene to a basic environment, where OH^- anions facilitated the deprotonation of -OH surface terminations, leading to the formation of -O terminations and water molecules.[41] In good agreement, the evolution of adsorbed H as H_2 gas also became more prominent after 40 cycles, coinciding with a marked decrease in the —(OH) and —O(OH) surface species.[29]

The reduction in hydroxyl terminations with increasing cycling indicated a transition from hydroxyl-rich to oxygen-terminated surfaces, which impacted the electrode's catalytic

© 2025 The Author(s). Small published by Wiley-VCH GmbH

16136829, 2025, 40, Downloaded from https://onlinelibrary.wiley.com/doi/10.1002/smll.202508259 by Ewha Womans University Library, Wiley Online Library on [13/01/2026]. See the Terms and Conditions (https://onlinelibrary.wiley.com/terms-and-conditions) on Wiley Online Library for rules of use; OA articles are governed by the applicable Creative Commons License

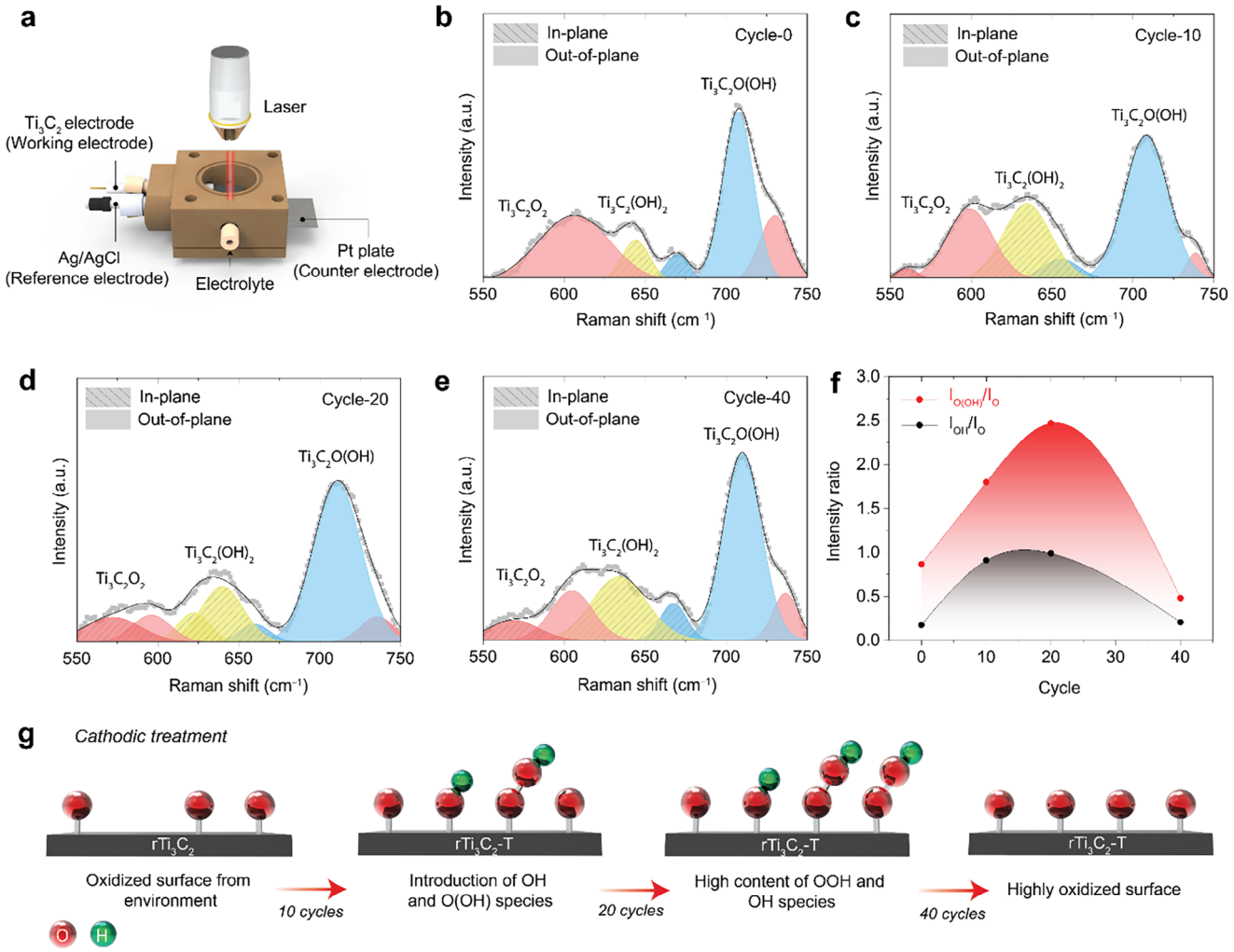


Figure 4. a) Schematic of Raman electrochemical cell for in situ monitoring of rTi_3C_2 catalyst during cathodic treatment in 0.1 M KOH. Representative, background-corrected in situ Raman spectra at selected wavenumbers, recorded on the negative potential from –0.1 to –0.4 V_{RHE} at b) 0, c) 10, d) 20, and e) 40 cycles. f) The intensity values recorded at $Ti_3C_2O(OH)$ and $Ti_3C_2(OH)_2$ intensity peaks normalized against $Ti_3C_2O_2$ intensity peaks. g) A simplified depiction of the incorporation of OOH and OH species into rTi_3C_2 MXene during the cathodic treatment.

activity as observed in the slight decrease in OER tests (Figure S7, Supporting Information). These findings were consistent with prior reports and suggested that hydroxyl ion intercalation under cathodic conditions plays a critical role in the conversion of $Ti_3C_2O_2$ to $Ti_3C_2O(OH)$ and $Ti_3C_2(OH)_2$.[19,34,40] Moreover, no significant shifts in the Raman band wavelengths of $Ti_3C_2O_2$, $Ti_3C_2O(OH)$, and $Ti_3C_2(OH)_2$ were observed throughout the electroactivation process (Figure S8, Supporting Information). Collectively, the enhanced OER activity of rTi_3C_2-T MXene in acidic media was closely linked to the increased presence of (oxy)hydroxide species. This correlation highlights the critical role of precise surface composition control in optimizing catalytic performance. Additionally, the surface modifications proved especially important for improving the efficiency of MXene-based materials in OER, as the newly formed (oxy)hydroxide species served as active sites, thereby enhancing OER performance.[42,43]

We then evaluated the OER performance of rTi_3C_2 and optimized rTi_3C_2-T MXenes in acidic media (0.5 M H_2SO_4). **Figure** 5a–c shows representative Raman spectra recorded at 0 (under OCV), 10, and 600 min during OER at 10 mA cm^{-2}, while Figure 5d summarizes key Raman peaks observed throughout the reaction. After 10 min, a significant increment in $Ti_3C_2O(OH)$ and $Ti_3C_2(OH)_2$ species was observed, indicated by an increase in the —O(OH) to =O ratio and —(OH) to =O ratio, respectively, suggesting initial surface oxidation of rTi_3C_2-T MXene catalyst. Extended testing of up to 600 min (Figure 5c; Figure S9, Supporting Information) revealed a gradual shift toward further oxidation, with the surface predominantly transitioning to $Ti_3C_2O_2$ species. This transformation indicates that prolonged OER cycling promotes the formation of a stable, oxide-rich layer easily. Consistent with previous reports, controlled anodic oxidation in $Ti_3C_2T_x$ electrodes increases interlayer spacing and induces pore formation, enhancing ion transport without depleting the electrochemically active oxygen species on the MXene surface.[44] Our observations align with this mechanism, where the oxide layer formation increased the electrode active surface

© 2025 The Author(s). Small published by Wiley-VCH GmbH

16136829, 2025, 40, Downloaded from https://onlinelibrary.wiley.com/doi/10.1002/smll.202508259 by Ewha Womans University Library, Wiley Online Library on [13/01/2026]. See the Terms and Conditions (https://onlinelibrary.wiley.com/terms-and-conditions) on Wiley Online Library for rules of use; OA articles are governed by the applicable Creative Commons License

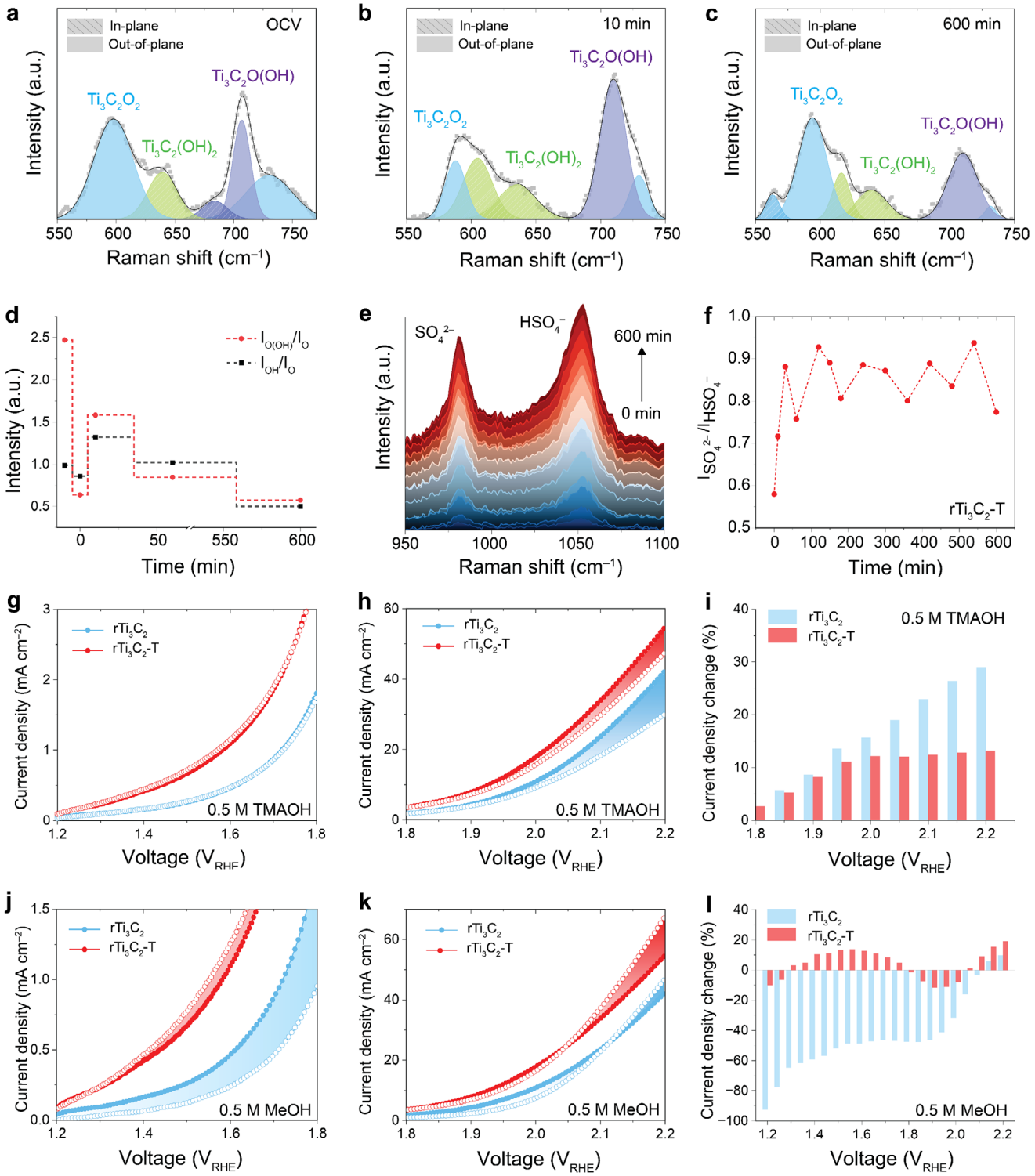


Figure 5. Representative background-corrected in situ Raman spectra at selected wavenumbers of rTi_3C_2-T (20 cycles), recorded during OER activities at 10 mA cm^{-2} in 0.5 M H_2SO_4 at a) OCV, b) 10 min, and c) 600 min. d) The $Ti_3C_2O(OH)$, $Ti_3C_2(OH)_2$ intensity peaks normalized against $Ti_3C_2O_2$ intensity peaks. e) The Raman bands of SO_4^{2-} at 960 cm^{-2} and HSO_4^- at 1040 cm^{-1} and f) corresponding intensity peaks analysis. OER intermediates probing of rTi_3C_2 and rTi_3C_2-T electrocatalyst in 0.5 M TMAOH- and 0.5 M MeOH-containing electrolyte g–l). The LSV curves at lower potential (g,j) and higher potential (h,k). The open and solid circle symbols represent the OER activities with and without TMAOH (MeOH) solution, respectively. (i,l) represents the current density change (%) over applied potential from 1.2–2.2 V_{RHE} in TMAOH- and MeOH-containing electrolyte, respectively.

© 2025 The Author(s). Small published by Wiley-VCH GmbH

16136829, 2025, 40, Downloaded from https://onlinelibrary.wiley.com/doi/10.1002/smll.202508259 by Ewha Womans University Library, Wiley Online Library on [13/01/2026]. See the Terms and Conditions (https://onlinelibrary.wiley.com/terms-and-conditions) on Wiley Online Library for rules of use; OA articles are governed by the applicable Creative Commons License

area, as reflected in the double-layer capacitance region (Figure S3, Supporting Information) and an elevated ECSA value of 43.1% (Figure 3g,h). Moreover, further analysis revealed changes in sulfate ions (SO_4^{2-}) over time (Figure 5e,f) in the rTi_3C_2-T electrode. The Raman bands of SO_4^{2-} at 960 cm^{-2} and HSO_4^- at 1040 cm^{-1} initially intensified and gradually stabilized during OER, indicating an increase in sulfate ion concentration. The increase likely results from HSO_4^- dissociation due to local proton accumulation from water oxidation, forming stronger hydrogen bonds between SO_4^{2-} and water molecules.[45] Sulfate ions have been reported to enhance the OER activity of metal-(oxy)hydroxide by accelerating catalyst reconstruction and stabilizing reaction intermediates during OER.[46]

2.4. OER Intermediates Probing and Theoretical Calculations

To further investigate the mechanistic pathways governing OER activity in rTi_3C_2 and rTi_3C_2-T electrodes, we employed targeted probing of reaction intermediates using 1) tetramethylammonium (TMA^+) to assess the presence of peroxo-like ($^*O_2^{-2}$) species indicative of the LOM,[47] and 2) methanol (MeOH) as a nucleophile to detect electrophilic $^*OH$ intermediates characteristic of the OPM. Figure 5g–l illustrates the variation in OER current density as a function of applied potential (1.2–2.2 V_{RHE}) in 0.5 M TMAOH- and 0.5 M MeOH-containing electrolytes, allowing differentiation between the active mechanistic pathways in each electrode, respectively. The interaction of TMA^+ with $^*O_2^{-2}$, led to a suppression of OER kinetics,[48] whereas MeOH oxidation indicated the detection of $^*OH$ intermediates, revealing mechanistic variations between the two systems.

For untreated rTi_3C_2, the absence of surface functionalization and the presence of abundant oxygen vacancies promoted preferential OH adsorption at defect sites. This inhibited direct OER activity, favoring defect filling via OH or O adsorption before oxygen evolution could proceed. Consequently, OER proceeded via the AEM at Ti–O sites, with $^*O$ to $^*OOH$ as the RDS and high overpotential of 1.6 V (**Figure 6a**). A control experiment conducted in the presence and absence of TMA^+ observed the stability of rTi_3C_2 under TMAOH up to 1.8 V_{RHE}, reaffirming AEM as the dominant mechanism. At higher potential (>1.8 V_{RHE}), however, a progressive suppression in current density from 2.01% to 28.9% at 2.2 V_{RHE} (Figure 5h) suggested increasing LOM involvement, where lattice oxygen ($^*O$) and oxygen vacancies (V_O) played an active role. Despite this, the theoretical calculations of LOM pathway in rTi_3C_2 exhibited a high overpotential of 2.9 V, with the RDS shifting from $^*O$ to $^*OOH$ formation (AEM) to molecular O_2 release ($^*OO \rightarrow O_2$) (Figure 6a). This value corroborates computational findings that predict a sluggish LOM pathway, necessitating higher energetic barriers. Additionally, rTi_3C_2-T displayed a smaller current suppression (≈13%) at 1.75–1.95 V_{RHE} and a more stable response at higher potentials, indicating that the LOM pathway is dominant in rTi_3C_2 and was mitigated in rTi_3C_2-T due to improved reaction kinetics.

The presence of $^*OH$ intermediates in the OPM pathway was further investigated using MeOH oxidation. This method offers sensitivity for detecting $^*OH$ intermediates, particularly in acidic electrolytes.[49] As depicted in Figure 5j,k, the OER current density variations in 0.5 M MeOH provided additional mechanistic insights. For rTi_3C_2, the presence of MeOH led to a negative shift in current density (Figure 5l). This suggests that MeOH disrupted lattice oxygen ($^*O$) and $^*OH$ intermediates, leading to surface poisoning and suppressed OER activity rather than facilitating methanol oxidation.

Conversely, rTi_3C_2-T exhibited a dynamic mechanistic transition, as evidenced by its sinusoidal current response between 1.2 and 2.2 V_{RHE} (Figures 5l and 6). The rTi_3C_2-T, enriched with surface (oxy)hydroxide species, exhibited AEM pathway with a reduced energy barrier. The overpotential for the RDS ($^*O \rightarrow {}^*OOH$) in AEM was reduced to 0.92 V, representing a 42.5% decrease compared to untreated rTi_3C_2, therefore contributing to the enhanced OER activity (Figure 6a). Moreover, at 1.3–1.8 V_{RHE}, the current density increased up to 13.7%, indicating OPM participation at a lower potential (Figure 5j). Between 1.8–2.0 V_{RHE}, a negative shift in current density suggested a transition toward LOM, where lattice oxygen ($^*O$) became increasingly reactive. This was further supported by the enhanced TMA^+ sensitivity observed in rTi_3C_2-T (Figure 5h). At >2.0 V_{RHE}, OPM re-emerged, driving an 18.9% increase in OER current density, underscoring the adaptive nature of rTi_3C_2-T, which transitions from AEM/OPM at lower potentials to a mixed LOM/OPM at higher potentials. Notably, the calculated OPM pathway in rTi_3C_2-T exhibited a reduced overpotential of 0.47 V, with the RDS shifting to adsorbed H_2O dissociation ($^*H_2O \rightarrow {}^*OH$), reinforcing its improved OER activity (Figure 6a). Electrostatic potential calculations further substantiated these findings. Compared to untreated rTi_3C_2 (Fermi level: 3.67 eV), rTi_3C_2-T exhibited a 19.7% shift in Fermi level (4.57 eV) (Figure 6c,d), effectively aligning the Ti 3d-electron density of states (DOS) with the Fermi level, therefore enhanced electron transfer between the surface and adsorbed intermediates, thus facilitating OER activities at active Ti sites.

We further corroborated our observations using *operando* FTIR spectroscopy, as shown in Figures S10 and S11 (Supporting Information). On the rTi_3C_2 surface, we observed lower vibration intensities associated with adsorbed $^*O$ (Ti–O) and $^*OH$ (M–OH) species against the treated rTi_3C_2 (rTi_3C_2-T), indicating a higher participation of the lattice oxygen mechanism (LOM).[50] The broad OH adsorption band observed on rTi_3C_2 further suggests the co-existence of the adsorbate evolution mechanism (AEM), as previously reported.[50] In contrast, rTi_3C_2-T exhibited a more intense and distinct Ti–O vibration band centered ≈600–700 cm^{-1}, which gradually increased and extended to 900 cm^{-1}, evidencing structural changes in Ti–O bonding. This spectral evolution aligns with the calculated OPM pathway, where the rate-determining step shifts toward adsorbed water dissociation ($^*H_2O \rightarrow {}^*OH$), contributing to the increased Ti–O peak intensity. Notably, rTi_3C_2-T displayed a prominent absorption peak at 1127.9 cm^{-1} with an accompanying shoulder at 1118.4 cm^{-1}. These features intensified substantially as the applied potential approached the OER region (>1.8 V), highlighting the accumulation of OER intermediates. The shoulder peak at 1118.4 cm^{-1}, assigned to O—O bond formation is linked to oxygen bridge formation between metal sites during OPM-type OER, as reported in previous studies.[51,52] These observations also closely match those reported by Lin et al (1128 and 1089 cm^{-1}).[11] The central peak at 1127.9 cm^{-1} is assigned to linearly bonded superoxo species (metal—O—O), known intermediates preceding O_2

© 2025 The Author(s). Small published by Wiley-VCH GmbH

16136829, 2025, 40, Downloaded from https://onlinelibrary.wiley.com/doi/10.1002/smll.202508259 by Ewha Womans University Library, Wiley Online Library on [13/01/2026]. See the Terms and Conditions (https://onlinelibrary.wiley.com/terms-and-conditions) on Wiley Online Library for rules of use; OA articles are governed by the applicable Creative Commons License

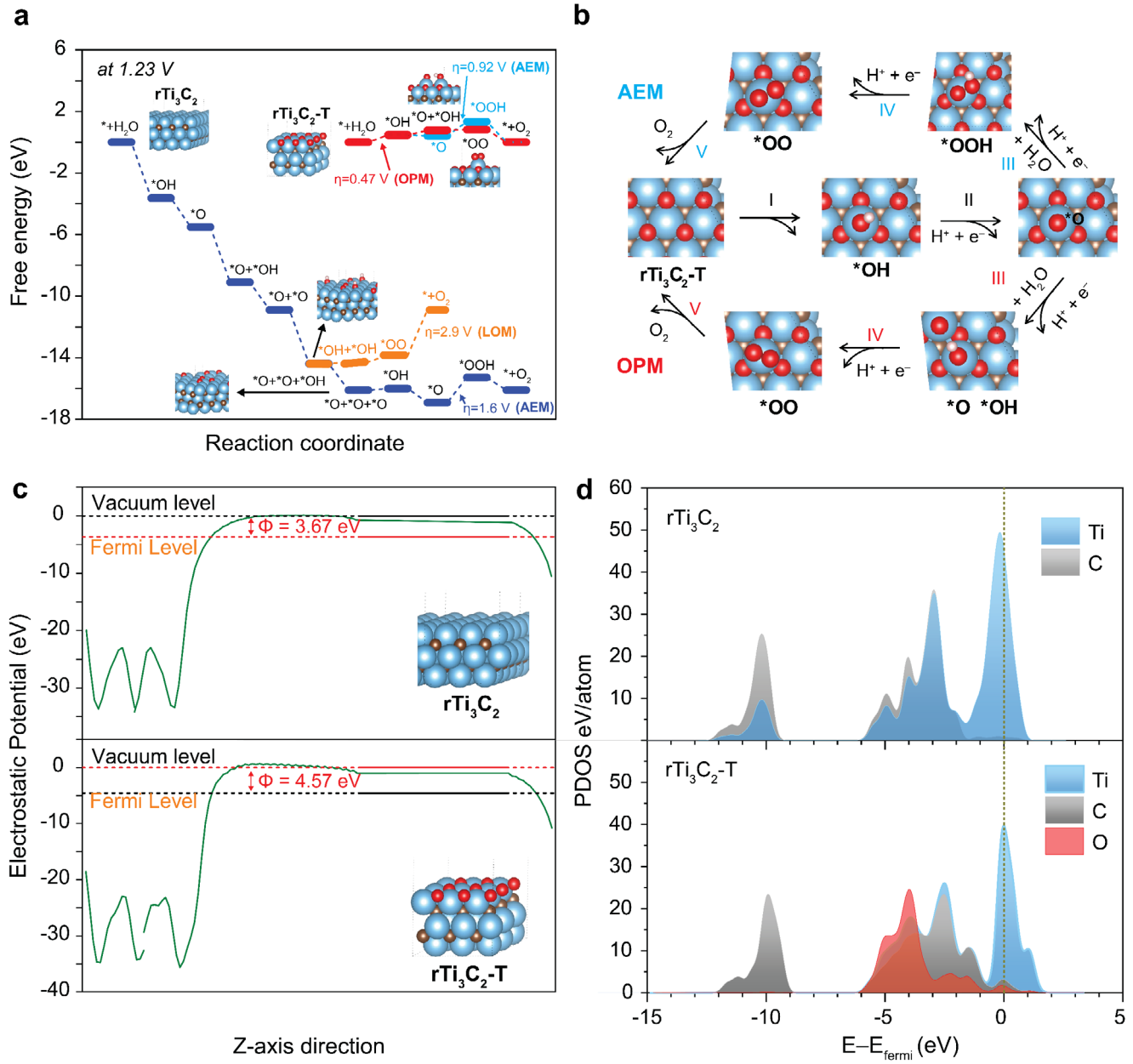


Figure 6. a) The free energy diagrams for preferred OER paths on the surfaces of untreated rTi_3C_2 and treated rTi_3C_2-T MXene. b) AEM and OPM paths of OER on the treated rTi_3C_2-T surface. c) Electrostatic potential of the surfaces of untreated rTi_3C_2 and treated rTi_3C_2-T. d) PDOS of untreated rTi_3C_2 and treated rTi_3C_2-T slab for Ti *3d*, C *2p*, and O *2p* bands. Corresponding Fermi level is denoted by a dashed line.

evolution.[53] In addition, the OH-related vibrational mode, the characteristic of OPM pathways was identified at 3649 cm^{-1} and exhibited a clear potential-dependent intensity increase.[11,54] The sharp increase in OH intensity and narrower peak width on rTi_3C_2-T further delineate the mechanistic divergence between the untreated and treated surfaces, reinforcing the role of surface reconstruction in steering the transition of OER mechanism pathways.

Overall, these findings highlight that rTi_3C_2-T outperforms rTi_3C_2 due to the synergistic contribution of AEM to OPM routes, leading to enhanced catalytic activity through optimized reaction kinetics and reduced overpotentials. This mechanistic understanding provides crucial insights into the role of surface modifications in tuning OER performance with improved activities.

3. Conclusion

This study investigates electro-activated reduced Ti_3C_2 MXene (rTi_3C_2) as a potential catalyst for modulating OER pathways through selective surface reconstruction. By modulating the population of surface (oxy)hydroxide species, rTi_3C_2 promotes the

© 2025 The Author(s). Small published by Wiley-VCH GmbH

16136829, 2025, 40, Downloaded from https://onlinelibrary.wiley.com/doi/10.1002/smll.202508259 by Ewha Womans University Library, Wiley Online Library on [13/01/2026]. See the Terms and Conditions (https://onlinelibrary.wiley.com/terms-and-conditions) on Wiley Online Library for rules of use; OA articles are governed by the applicable Creative Commons License

transition from AEM to OPM route, leading to a 27% reduction in overpotential at 10 mA cm^{-2} and a 67% increase in current density at high voltages compared to the pristine Ti_3C_2. Experimental measurements and *operando* vibrational spectroscopy reveal a dynamic interplay between surface functional groups and reaction intermediates, highlighting the role of electrochemical conditioning in tuning active sites. First-principles calculations further validate a cooperative catalysis mechanism with a reduced energy barrier, corroborating the enhanced activity of our (oxy)hydroxide-rich MXene catalyst. These findings deepen our understanding of how electrochemical activation and surface reconstruction influence the OER mechanism pathway, offering a framework for optimizing OER performance through tailored surface catalyst design. Further studies on structural modifications and electrolyte conditions could refine the AEM/OPM transition, contributing to the development of more efficient MXene-based catalysts for sustainable energy applications.

Supporting Information

Supporting Information is available from the Wiley Online Library or from the author.

Acknowledgements

This work was supported by the National Research Foundation of Korea funded by the Ministry of Education (2021R1A6A1A10039823; RS-2025-02982993), and by the Korea Basic Science Institute (National Research Facilities and Equipment Center) grant funded by the Ministry of Education (2020R1A6C101B194). J.K. acknowledges the financial support from the National Research Foundation of Korea (NRF) grant funded by the Korea government (MSIT) (No. RS-2023-00212105). This research was supported by the Basic Science Research Program through the National Research Foundation of Korea (NRF) funded by the Ministry of Education (RS-2024-00461946). C.Y. acknowledges the support from the National Natural Science Foundation of China (52473235), Guangdong Basic and Applied Basic Research Foundation (2022A1515110628), High Level of Special Funds (G03050K002), and Guangdong Provincial Key Laboratory of Computational Science and Material Design (2019B030301001). Computing resources were supported by the Center for Computational Science and Engineering at Southern University of Science and Technology.

Conflict of Interest

The authors declare no conflict of interest.

Author Contributions

J.K., F.M.M., and D.H.K. supervised the overall project. N.A.R.C.M. was responsible for developing concrete strategies, materials synthesis, characterization, electrochemical testing, and related data processing. J.K. and H.L. supported structural analysis using ex situ and *operando* Raman measurements and related data processing. M.G., C.Y., and Y.B. performed the theoretical and simulation study. N.A.R.C.M., H.L., M.G., C.Y., Y.B., Z.L., J.K., F.M.M., and D.H.K. wrote the manuscript. All the authors have read and approved the final manuscript.

Data Availability Statement

The data that support the findings of this study are available from the corresponding author upon reasonable request.

Keywords

electrocatalyst, MXene, OER, oxyhydroxides, Ti_3C_2

Received: July 9, 2025
Published online: August 22, 2025

[1] B. Anasori, M. R. Lukatskaya, Y. Gogotsi, *Nat. Rev. Mater.* **2017**, *2*, 16098.
[2] S. Bai, M. Yang, J. Jiang, X. He, J. Zou, Z. Xiong, G. Liao, S. Liu, *npj 2D Mater. Appl.* **2021**, *5*, 78.
[3] H. T. Das, T. E. Balaji, S. Dutta, N. Das, T. Maiyalagan, *Int. J. Energy Res.* **2022**, *46*, 8625.
[4] P. Eghbali, A. Hassani, S. Wacławek, K.-Y. A. Lin, Z. Sayyar, F. Ghanbari, *Chem. Eng. J.* **2024**, *480*, 147920.
[5] X. Pan, X. Yang, M. Yu, X. Lu, H. Kang, M.-Q. Yang, Q. Qian, X. Zhao, S. Liang, Z. Bian, *Nat. Commun.* **2023**, *14*, 4183.
[6] Y. Sun, J. Lee, N. H. Kwon, J. Lim, X. Jin, Y. Gogotsi, S.-J. Hwang, *ACS Nano* **2024**, *18*, 6243.
[7] J. Zhang, Y. Zhao, X. Guo, C. Chen, C.-L. Dong, R.-S. Liu, C.-P. Han, Y. Li, Y. Gogotsi, G. Wang, *Nat. Catal.* **2018**, *1*, 985.
[8] T. Hou, Q. Luo, Q. Li, H. Zu, P. Cui, S. Chen, Y. Lin, J. Chen, X. Zheng, W. Zhu, S. Liang, J. Yang, L. Wang, *Nat. Commun.* **2020**, *11*, 4251.
[9] M. Retuerto, L. Pascual, F. Calle-Vallejo, P. Ferrer, D. Gianolio, A. G. Pereira, Á. García, J. Torrero, M. T. Fernández-Díaz, P. Bencok, M. A. Peña, J. L. G. Fierro, S. Rojas, *Nat. Commun.* **2019**, *10*, 2041.
[10] Q. Ma, S. Mu, *Interdiscip. Mater.* **2023**, *2*, 53.
[11] C. Lin, J.-L. Li, X. Li, S. Yang, W. Luo, Y. Zhang, S.-H. Kim, D.-H. Kim, S. S. Shinde, Y.-F. Li, Z.-P. Liu, Z. Jiang, J.-H. Lee, *Nat. Catal.* **2021**, *4*, 1012.
[12] C. Rong, X. Huang, H. Arandiyan, Z. Shao, Y. Wang, Y. Chen, *Adv. Mater.* **2025**, *37*, 2416362.
[13] Y. Zhang, H. Zhang, A. Liu, C. Chen, W. Song, J. Zhao, *J. Am. Chem. Soc.* **2018**, *140*, 3264.
[14] F. L.e Formal, E. Pastor, S. D. Tilley, C. A. Mesa, S. R. Pendlebury, M. Grätzel, J. R. Durrant, *J. Am. Chem. Soc.* **2015**, *137*, 6629.
[15] J. Lee, A. Kumar, T. Yang, X. Liu, A. R. Jadhav, G. H. Park, Y. Hwang, J. Yu, C. T. K. Nguyen, Y. Liu, S. Ajmal, M. G. Kim, H. Lee, *Energy Environ. Sci.* **2020**, *13*, 5152.
[16] W. H. Lee, M. H. Han, Y.-J. Ko, B. K. Min, K. H. Chae, H.-S. Oh, *Nat. Commun.* **2022**, *13*, 605.
[17] S. Kumar, D. Kang, H. Hong, M. A. Rehman, Y. Lee, N. Lee, Y. Seo, *RSC Adv.* **2020**, *10*, 41837.
[18] N. Liu, Q. Li, H. Wan, L. Chang, H. Wang, J. Fang, T. Ding, Q. Wen, L. Zhou, X. Xiao, *Nat. Commun.* **2022**, *13*, 5551.
[19] A. Sarycheva, Y. Gogotsi, *Chem. Mater.* **2020**, *32*, 3480.
[20] M. Naguib, O. Mashtalir, M. R. Lukatskaya, B. Dyatkin, C. Zhang, V. Presser, Y. Gogotsi, M. W. Barsoum, *Chem. Commun.* **2014**, *50*, 7420.
[21] T. Hu, J. Wang, H. Zhang, Z. Li, M. Hu, X. Wang, *Phys. Chem. Chem. Phys.* **2015**, *17*, 9997.
[22] D. Liu, T. Li, W. Sun, W. Zhou, G. Zhang, *ACS Omega* **2022**, *7*, 31945.
[23] M. Lounasvuori, T. Zhang, Y. Gogotsi, T. Petit, *J. Phys. Chem. C* **2024**, *128*, 2803.
[24] T. Parker, D. Zhang, D. Bugallo, K. Shevchuk, M. Downes, G. Valurouthu, A. Inman, B. Chacon, T. Zhang, C. E. Shuck, Y.-J. Hu, Y. Gogotsi, *Chem. Mater.* **2024**, *36*, 8437.
[25] S. Chen, Y. Xiang, M. K. Banks, C. Peng, W. Xu, R. Wu, *Nanoscale* **2018**, *10*, 20043.
[26] K. M. Kang, D. W. Kim, C. E. Ren, K. M. Cho, S. J. Kim, J. H. Choi, Y. T. Nam, Y. Gogotsi, H.-T. Jung, *ACS Appl. Mater. Interfaces* **2017**, *9*, 44687.

© 2025 The Author(s). Small published by Wiley-VCH GmbH

16136829, 2025, 40, Downloaded from https://onlinelibrary.wiley.com/doi/10.1002/smll.202508259 by Ewha Womans University Library, Wiley Online Library on [13/01/2026]. See the Terms and Conditions (https://onlinelibrary.wiley.com/terms-and-conditions) on Wiley Online Library for rules of use; OA articles are governed by the applicable Creative Commons License

[27] P. Urbankowski, B. Anasori, T. Makaryan, D. Er, S. Kota, P. L. Walsh, M. Zhao, V. B. Shenoy, M. W. Barsoum, Y. Gogotsi, *Nanoscale* **2016**, *8*, 11385.
[28] Y. Jiang, T. Sun, X. Xie, W. Jiang, J. Li, B. Tian, C. Su, *ChemSusChem* **2019**, *12*, 1368.
[29] Y. Zou, S. A. Kazemi, G. Shi, J. Liu, Y. Yang, N. M. Bedford, K. Fan, Y. Xu, H. Fu, M. Dong, M. Al-Mamun, Y. L. Zhong, H. Yin, Y. Wang, P. Liu, H. Zhao, *EcoMat* **2023**, *5*, 12274.
[30] Q. Zhao, Y. Zhang, C. Ke, W. Yang, J. Yue, X. Yang, W. Xiao, *Nanoscale* **2024**, *16*, 8020.
[31] Z. Lv, W. Ma, M. Wang, J. Dang, K. Jian, D. Liu, D. Huang, *Adv. Funct. Mater.* **2021**, *31*, 2102576.
[32] S. Li, H. Chai, L. Zhang, Y. Xu, Y. Jiao, J. Chen, *J. Colloid Interface Sci.* **2023**, *642*, 235.
[33] H. Hong, H. Y. Kim, W. I.l Cho, H. C. Song, H. C. Ham, K. Chae, F. M. Mota, J. Y. Kim, D. H. Kim, *J. Mater. Chem. A* **2023**, *11*, 5328.
[34] J. Xia, S.-Z. Yang, B. Wang, P. Wu, I. Popovs, H. Li, S. Irle, S. Dai, H. Zhu, *Nano Energy* **2020**, *72*, 104681.
[35] C. L. Bentley, M. Kang, P. R. Unwin, *J. Am. Chem. Soc.* **2019**, *141*, 2179.
[36] Z. W. Seh, J. Kibsgaard, C. F. Dickens, I. Chorkendorff, J. K. Nørskov, T. F. Jaramillo, *Science* **2017**, *355*, aad4998.
[37] S. Zhu, R. Yang, H. J. W. Li, S. Huang, H. Wang, Y. Liu, H. Li, T. Zhai, *Angew. Chem., Int. Ed.* **2024**, *63*, 202319462.
[38] M. Zhou, Q. Weng, X. Zhang, X. Wang, Y. Xue, X. Zeng, Y. Bando, D. Golberg, *J. Mater. Chem. A* **2017**, *5*, 4335.
[39] X. Zheng, B. Zhang, P. De Luna, Y. Liang, R. Comin, O. Voznyy, L. Han, F. P. García de Arquer, M. Liu, C. T. Dinh, T. Regier, J. J. Dynes, S. He, H. L. Xin, H. Peng, D. Prendergast, X. Du, E. H. Sargent, *Nat. Chem.* **2018**, *10*, 149.
[40] M. Jeong, S. Park, T. Kwon, M. Kwon, S. Yuk, S. Kim, C. Yeon, C.-W. Lee, D. Lee, *ACS Appl. Mater. Interfaces* **2024**, *16*, 34798.
[41] V. Natu, R. Pai, O. Wilson, E. Gadasu, H. Badr, A. Karmakar, A. J. D. Magenau, V. Kalra, M. W. Barsoum, *Chem. Mater.* **2022**, *34*, 678.
[42] M. Chen, D. Liu, J. Feng, P. Zhou, L. Qiao, W. Feng, Y. Chen, K. W. Ng, S. Wang, W. F. Ip, H. Pan, *Chem. Eng. J.* **2022**, *443*, 136432.
[43] W. Yang, C. Zhang, B. Jiang, P. Wang, L. Yan, L. Hou, F. Yang, Y. Li, *Chem. Eng. J.* **2022**, *434*, 134473.
[44] J. Tang, T. S. Mathis, N. Kurra, A. Sarycheva, X. Xiao, M. N. Hedhili, Q. Jiang, H. N. Alshareef, B. Xu, F. Pan, Y. Gogotsi, *Angew. Chem., Int. Ed.* **2019**, *58*, 17849.
[45] Y. Sui, M. Yu, Y. Xu, X. Ji, *J. Electrochem. Soc.* **2022**, *169*, 030537.
[46] H. Liao, T. Luo, P. Tan, K. Chen, L. Lu, Y. Liu, M. Liu, J. Pan, *Adv. Funct. Mater.* **2021**, *31*, 2102772.
[47] N. Yao, H. Jia, J. Zhu, Z. Shi, H. Cong, J. Ge, W. Luo, *Chem* **2023**, *9*, 1882.
[48] Z.-F. Huang, J. Song, Y. Du, S. Xi, S. Dou, J. M. V. Nsanzimana, C. Wang, Z. J. Xu, X. Wang, *Nat. Energy* **2019**, *4*, 329.
[49] H. B. Tao, Y. Xu, X. Huang, J. Chen, L. Pei, J. Zhang, J. G. Chen, B. Liu, *Joule* **2019**, *3*, 1498.
[50] Y. Hu, Y. Zheng, J. Jin, Y. Wang, Y. Peng, J. Yin, W. Shen, Y. Hou, L. Zhu, L. An, M. Lu, P. Xi, C.-H. Yan, *Nat. Commun.* **2023**, *14*, 1949.
[51] C. Lang, J. Li, K. R. Yang, Y. Wang, D. He, J. E. Thorne, S. Croslow, Q. Dong, Y. Zhao, G. Prostko, G. W. Brudvig, V. S. Batista, M. M. Waegele, D. Wang, *Chem* **2021**, *7*, 2101.
[52] B. Wang, K. Zhao, Z. Yu, C. Sun, Z. Wang, N. Feng, L. Mai, Y. Wang, Y. Xia, *Energy Environ. Sci.* **2020**, *13*, 2200.
[53] J. P. Vivek, N. G. Berry, J. Zou, R. J. Nichols, L. J. Hardwick, *J. Phys. Chem. C* **2017**, *121*, 19657.
[54] H. Su, W. Zhou, H. Zhang, W. Zhou, X. Zhao, Y. Li, M. Liu, W. Cheng, Q. Liu, *J. Am. Chem. Soc.* **2020**, *142*, 12306.

© 2025 The Author(s). Small published by Wiley-VCH GmbH

16136829, 2025, 40, Downloaded from https://onlinelibrary.wiley.com/doi/10.1002/smll.202508259 by Ewha Womans University Library, Wiley Online Library on [13/01/2026]. See the Terms and Conditions (https://onlinelibrary.wiley.com/terms-and-conditions) on Wiley Online Library for rules of use; OA articles are governed by the applicable Creative Commons License